

Mechanical and magnetic properties of Mn-Pt compounds and nanocompositesT. Káňa^{1,*} and M. Šob^{2,1,3,†}¹*Institute of Physics of Materials, Academy of Sciences of the Czech Republic, Žitkova 22, CZ-616 62 Brno, Czech Republic*²*Central European Institute of Technology, CEITEC MU, Masaryk University, Kamenice 5, CZ-625 00 Brno, Czech Republic*³*Department of Chemistry, Faculty of Science, Masaryk University, Kotlářská 2, CZ-611 37 Brno, Czech Republic*

(Received 17 August 2011; revised manuscript received 2 May 2012; published 28 June 2012)

An analysis of mechanical and magnetic properties of Mn-Pt compounds and nanocomposites is provided using *ab initio* electronic structure calculations. Adding manganese to platinum matrix reduces the bulk modulus and enhances the Young moduli E_{100} and E_{111} and shear moduli $(c_{11} - c_{12})/2$ and c_{44} . With increasing Mn content, the theoretical tensile and compressive strengths are also enhanced. On the whole, manganese addition makes the Mn-Pt compounds softer but increases their resistance to shape deformation. Many of these compounds may be considered natural linear nanocomposites. We studied the magnetic configurations of recently found MnPt₇ ordered structure and predict an antiferromagnetic state with spins altering along the [100] direction to be the ground state of this compound. Our calculation further predicts antiferromagnetic ordering of MnPt₇ below 265 K and confirms the experimental findings that Mn atoms in a Pt matrix preferentially occupy corners and centers of faces of the $2 \times 2 \times 2$ Pt supercell. We further propose structures of Mn-Pt nanocomposites exhibiting the composition of MnPt₁₅ and identify a structure with an antiferromagnetic ordering with spins altering along the [100] direction as the ground state of the MnPt₁₅ nanocomposite. We conclude that structures with lower manganese concentrations exhibit mostly antiferromagnetic ordering, while additional Mn atoms exceeding the atomic concentration of MnPt₇ (12.5 at%) build up locally atomic configurations of the MnPt₃ type with predominantly ferromagnetic interactions.

DOI: [10.1103/PhysRevB.85.214438](https://doi.org/10.1103/PhysRevB.85.214438)

PACS number(s): 62.25.-g, 71.15.Nc, 75.75.-c

I. INTRODUCTION

Adding manganese to platinum crystals and nanocrystals strongly affects their mechanical, magnetic, and catalytic properties.¹ For example, the ferromagnetic (FM) MnPt₃ compound exhibits a giant magneto-optical Kerr effect.² A nanocomposite consisting of self-assembled Mn-Pt nanocubes of average edge length 7.7 nm was recently synthesized by dissolving platinum acetate Pt(acac)₂ in either benzyl ether or phenyl ether in the presence of oleic acid and oleylamine, injecting a dimanganese decacarbonyl Mn₂(CO)₁₀ stock solution at 160 °C, and heating at 200–205 °C.³ It was shown that the catalytic activity of (100) facets of Mn-Pt nanocubes in an oxygen reduction reaction is higher than that of (111) facets and also higher than that of elemental Pt. Further, Mn-Pt nanocubes are particularly promising for methanol oxidation. The nanocubes, as synthesized, were chemically disordered, with Mn and Pt in an fcc unit cell of the A1 phase. After annealing, the nanocube structure was converted into the L1₂ phase of MnPt₃.

Another experimental study of Mn-Pt nanoparticles⁴ revealed the coexistence of a hard magnetic phase with a soft one. The hard magnetic phase has been attributed to the L1₂ phase of MnPt₃, while the soft magnetic phase was associated with the disordered fcc A1 phase. It is known that magnetic interactions between individual Mn atoms can establish a long-range ordered structure, as, for example, in a bulk crystal of α -manganese with 58 atoms in the unit cell.⁵ Detailed studies of magnetic interactions between individual Mn atoms in Mn clusters^{6–9} and nanowires^{10–12} have been performed in order to understand the underlying physics. The experimentally measured equilibrium distance of manganese atoms in the Mn dimer¹³ varies between 3.2 and 3.6 Å, depending on the spin multiplicity. The ground state of Mn

dimer is antiferromagnetic (AFM).^{14–16} If other atoms are located close to the Mn atoms, coupling of Mn spins can occur. Recent calculations of a Mn dimer on a CuN surface¹⁷ have shown that Mn spins may be coupled through the nitrogen atom.

Here, we are particularly interested in magnetic interactions between Mn atoms in an fcc platinum matrix. Our interest also concerns the mechanical properties of such structures. In contrast to Mn clusters, Mn atoms in Pt-rich Mn-Pt alloys stand mutually in the positions of second or third nearest neighbors or they are even more distant. This is due to the good solubility of Mn in Pt.¹⁸ We regard such Mn-Pt structures as linear nanocomposites. The reason for this can be seen in Fig. 1, which presents the recently found MnPt₇ structure that can be described with the help of a $2 \times 2 \times 2$ Pt supercell with Mn atoms located at the corners and in the centers of the faces of the supercell (henceforth called fcc positions). It may also be described in terms of alternating (111) planes of pure Pt and (111) planes of MnPt₃. Finally, it represents a natural linear nanocomposite if we consider the structure as an assembly of striped Mn nanochains embedded in an fcc Pt matrix. Here, the nanochains are oriented along the $\langle 110 \rangle$ or $\langle 100 \rangle$ directions (see Fig. 1). The MnPt₇ structure was first found in the form of a thin film¹⁹ and later as a bulk crystal.^{20–22}

The MnPt₃ structure may be regarded as an assembly of Mn nanochains oriented along the $\langle 100 \rangle$ directions in the embedding fcc platinum matrix. MnPt₃ is FM with a Curie temperature T_C of 380 K,^{23,24} and due to its large magneto-optical Kerr effect, it is regarded as a promising candidate for a high-density magneto-optical storage medium.^{25,26} However, chemical disorder destroys its ferromagnetism. Some of the mechanical and magnetic properties of MnPt₃ were recently calculated in Refs. 27 and 28.

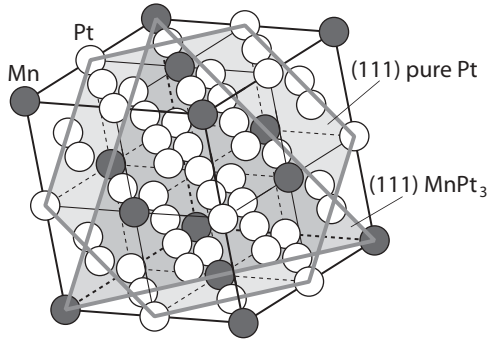


FIG. 1. The MnPt_7 structure may be described by a $2 \times 2 \times 2$ platinum supercell with the Mn atoms located at the fcc positions in this supercell. Mn atoms are represented by black spheres, and Pt atoms by white spheres.

If we lower the Mn content in the Pt matrix we may arrive at a Mn-Pt alloy with 8.8 at% Mn that was experimentally studied in Ref. 29. Measurements have shown its magnetic spin glass behavior. AFM interactions dominate in this alloy and the spin structure is modulated along the $[100]$ direction, with the wavelength being twice as large as the chemical unit cell.

For these and lower concentrations of Mn atoms in a Pt matrix, we propose three model ordered structures with the stoichiometry of MnPt_{15} , i.e., with a Mn content of 6.25 at%. Similarly to the MnPt_7 structure, they can also be regarded as natural linear nanocomposites. In our three models of MnPt_{15} , the nanochains are oriented along the $[100]$, $\langle 110 \rangle$, and $\langle 111 \rangle$ directions (see Fig. 5).

The purpose of this work is to study, from first principles, the mechanical and magnetic properties of ordered Mn-Pt compounds and nanocomposites. The paper is organized as follows. After providing computational details in Sec. II, we present the elemental Pt, MnPt_3 , MnPt_7 , and MnPt_{15} structures in Sec. III and calculate their elastic constants, theoretical tensile and compressive strengths, and maximum corresponding strains in the $\langle 100 \rangle$ and $\langle 111 \rangle$ directions. For MnPt_7 , we discuss the effect of its magnetic ordering on these values. Further, we briefly discuss the interplay between the structure and the magnetism of MnPt_{15} linear nanocomposites. Concluding Sec. IV then summarizes the results.

II. COMPUTATIONAL DETAILS

For total-energy calculations, we employed the full-potential linearized augmented-plane wave (FLAPW) method implemented in the WIEN2k code.³⁰ For the exchange-correlation energy, we used the local density approximation,³¹ as this approximation fits better for Pt and its compounds.²⁷ The muffin-tin radii of 2.4 a.u. of Pt atoms and 2.2 a.u. of Mn atoms were kept constant for all calculations. The number of k points in the whole Brillouin zone was equal to 20 000 for the fcc structure of elemental Pt and was correspondingly reduced for structures with a larger number of atoms to have the same density of k points for all structures studied. The product of the muffin-tin radius and the maximum reciprocal space vector, $R_{\text{MT}}k_{\text{max}}$, was equal to 8.8, and the maximum value of ℓ for the waves inside the atomic spheres, ℓ_{max} , was

set to 10. The largest reciprocal vector $|\mathbf{G}|$ in the charge Fourier expansion, G_{max} , was equal to 16. In order to treat the semicore states correctly, the augmented plane wave plus local-orbital extension³² was used. The energy convergence criterion was 2×10^{-5} eV/atom, and on the basis of the convergence tests with respect to the number of k points and the parameter $R_{\text{MT}}k_{\text{max}}$, the error in the calculated total energies may be estimated to be less than 8×10^{-4} eV/atom. The spin-orbit coupling was not included and our calculations are restricted to collinear magnetism. The values of calculated magnetic moments at individual atoms correspond to electrons inside the muffin-tin spheres.

III. RESULTS AND DISCUSSION

A. Elemental Pt

At first, we were interested in the mechanical properties of the platinum matrix itself. We determined the bulk modulus B , elastic constants c_{11} , c_{12} , and c_{44} , and Young moduli E_{100} and E_{111} of elemental platinum in the directions $\langle 100 \rangle$ and $\langle 111 \rangle$. The values of Young moduli E_{100} and E_{111} are given in Ref. 33 as

$$E_{100} = \frac{(c_{11} - c_{12})(c_{11} + 2c_{12})}{c_{11} + c_{12}}$$

and

$$E_{111} = \frac{3c_{44}(c_{11} + 2c_{12})}{c_{44} + c_{11} + 2c_{12}}.$$

According to Refs. 34 and 35, we have calculated the maximum uniaxial tensile and compressive stress (theoretical tensile and compressive strength) $\sigma_{\text{max},0}$ at zero biaxial stress and the corresponding maximum strain $\varepsilon_{\text{max},0}$ for Pt in the $\langle 100 \rangle$ and $\langle 111 \rangle$ directions. Our values are presented in Table I. They agree well with experimental data³⁶ and previous results in Refs. 37–39.

In the $\langle 111 \rangle$ direction, the maximum compressive stress of Pt is 1.29 times higher than the maximum tensile stress in this direction. In addition to that, the uniaxial

TABLE I. Lattice constant a , bulk modulus B , elastic constants c_{11} , c_{12} , and c_{44} , Young moduli E_{100} and E_{111} , theoretical tensile and compressive strengths $\sigma_{\text{max},0}$, and corresponding strains $\varepsilon_{\text{max},0}$ in elemental Pt. Positive values of $\sigma_{\text{max},0}$ and $\varepsilon_{\text{max},0}$ correspond to a tension; negative values, to a compression.

	This work	Exp. ³⁶	Other DFT ^{37,38}
a (Å)	3.914	3.924	3.91
B (GPa)	317.0	282.7	
c_{11} (GPa)	391.6	346.7	
c_{12} (GPa)	279.7	250.7	
c_{44} (GPa)	82.5	76.5	
$(c_{11} - c_{12})/2$ (GPa)	56	48	
E_{100} (GPa)	159	136	149
E_{111} (GPa)	228	211	219
$\sigma_{\text{max},0} \langle 100 \rangle$ (GPa)	34.72 (−7.83)		34.1 (−7.51) ^a
$\varepsilon_{\text{max},0} \langle 100 \rangle$ (GPa)	0.324 (−0.114)		0.34
$\sigma_{\text{max},0} \langle 111 \rangle$ (GPa)	28.33 (−37.31)		29.9
$\varepsilon_{\text{max},0} \langle 111 \rangle$ (GPa)	0.234 (−0.156)		0.25

^aFrom Ref. 39.

tension-compression asymmetry is even larger for the $\langle 100 \rangle$ direction, where the maximum tensile stress $\sigma_{\max,0}$ in compression is almost 4.5 times lower than the $\sigma_{\max,0}$ in tension. The low value of compressive strength in the $\langle 100 \rangle$ direction is in very good agreement with other calculations³⁹ and can be related to the height of energy barrier between the fcc and the bcc phase within the Bain path for Pt. The calculations in Ref. 39 even suggested that Pt nanowires thinner than 1.39 nm should exhibit a spontaneous relaxation to the body-centered tetragonal (bct) phase due to their surface stress.

B. MnPt₃

The L1₂ (AuCu₃) structure of the MnPt₃ intermetallic compound may also be understood as a dense packing of Mn nanochains along the $\langle 100 \rangle$ direction embedded in the Pt matrix. Table II presents the bulk modulus B , elastic constants, Young moduli E_{100} and E_{111} , and theoretical tensile or compressive strength in the $\langle 100 \rangle$ and $\langle 111 \rangle$ directions. Compared to the elemental platinum matrix, the lattice constant of MnPt₃ is lowered by 1.3% (Fig. 7) and the bulk modulus B decreases by about 15% (Fig. 8). On the other hand, we note a strong enhancement of the shear moduli $(c_{11} - c_{12})/2$ and c_{44} , by 46% and 71%, and the Young moduli E_{100} and E_{111} , by 41% and 57%, respectively.

Comparing the values of maximum compressive stress in the $\langle 100 \rangle$ direction for MnPt₃ and elemental Pt (Tables I and II and Figs. 3 and 9), we see that the addition of manganese to the Pt matrix substantially enhances its compressive strength $\sigma_{\max,0} \langle 100 \rangle$, by 111%, and thus reduces its uniaxial tension-compression asymmetry. The reason for this stems from the fact that the Mn sublattice in MnPt₃ does not tend to transform from an fcc structure into a bcc or bct structure when compressed in the $\langle 100 \rangle$ direction as was the case for the fcc platinum metal. The eventually squeezed Mn sublattice in MnPt₃ changes from a simple cubic to a simple tetragonal structure for all deformations $\varepsilon \langle 100 \rangle$. The enhancement of the maximum compressive stress $\sigma_{\max,0} \langle 111 \rangle$ with respect to elemental Pt is 23%, whereas the enhancement of the maximum tensile stress in both directions is somewhat less

TABLE II. Lattice constant a , bulk modulus B , elastic constants c_{11} , c_{12} , and c_{44} , Young moduli E_{100} and E_{111} , theoretical tensile and compressive strengths $\sigma_{\max,0}$, and corresponding maximum strains $\varepsilon_{\max,0}$ in MnPt₃. Positive values of $\sigma_{\max,0}$ and $\varepsilon_{\max,0}$ correspond to a tension; negative values, to a compression.

	This work	Exp. ⁴³	Ref. 27
a (Å)	3.863	3.893	3.860
B (GPa)	268.2		265.5
c_{11} (GPa)	377.8		370.3
c_{12} (GPa)	213.3		219.8
c_{44} (GPa)	140.7		129.5
$(c_{11} - c_{12})/2$ (GPa)	82		75
E_{100} (GPa)	224		207
E_{111} (GPa)	359		335
$\sigma_{\max,0} \langle 100 \rangle$ (GPa)	37.20 (−16.53)		
$\varepsilon_{\max,0} \langle 100 \rangle$ (GPa)	0.310 (−0.120)		
$\sigma_{\max,0} \langle 111 \rangle$ (GPa)	32.80 (−45.95)		
$\varepsilon_{\max,0} \langle 111 \rangle$ (GPa)	0.221 (−0.136)		

pronounced: 7% for $\sigma_{\max,0} \langle 100 \rangle$ and 16% for $\sigma_{\max,0} \langle 111 \rangle$. The tension-compression asymmetry for MnPt₃ in the $\langle 100 \rangle$ direction is reduced by approximately twice in comparison with that for elemental Pt. A more detailed discussion of elastic behavior is presented in Sec. III E.

The calculated magnetic moments inside the muffin-tin spheres of Mn amount to 3.562 μ_B and there is an induced magnetic moment of 0.152 μ_B at Pt atoms. The calculated total magnetic moment per formula unit (f.u.) equals 4.126 μ_B and the magnetic moment of electrons in the interstitial region is 0.108 μ_B . There is good agreement with the values obtained from polarized neutron experiments⁴⁰ on MnPt₃ at 77 K. They showed a magnetic moment of $0.17 \pm 0.04 \mu_B$ at Pt sites and $3.60 \pm 0.09 \mu_B$ at Mn sites and a total magnetic moment of $4.11 \pm 0.21 \mu_B$ per unit cell. Similar values of magnetic moments in MnPt₃ have been calculated elsewhere^{27,28,42} too.

The experimental magnetic ground state of MnPt₃ is FM. Reference 28 deals with an alternative AFM ordering that exhibits the opposite orientation of magnetic moments in the alternative (110) planes containing Mn atoms. This AFM ordering was calculated to have an energy only 15 meV/atom higher than that of the ground-state FM ordering. Further, if the magnetic moments have opposite orientations on alternating (100) planes containing Mn atoms, the calculated energy increases by 35 meV/atom more than the energy of the FM ground state. Thus, in our calculations, we deal only with the FM ordering of MnPt₃.

C. MnPt₇

The recently found (linear) nanocomposite MnPt₇^{19–22} is displayed in Fig. 1. Apart from the fully ordered structure, disordered structures can be found where Mn atoms can also occupy the sites at the centers of the $2 \times 2 \times 2$ supercell edges. The experimental lattice constant for Mn_{0.119}Pt_{0.881} is 3.912 Å.²¹ This Mn concentration is very close to MnPt₇.

We have considered three possible types of magnetic ordering in MnPt₇. The first is the FM one and the remaining two are the AFM orderings, AFM [100] [Fig. 2(a)] and AFM [111] [Fig. 2(b)], with opposite orientations of magnetic moments in the alternative (100) and (111) planes, respectively. The magnetic moments in the FM ordering were calculated to be 3.769 μ_B on Mn atoms, 0.171 μ_B induced on Pt atoms in the centers of the $2 \times 2 \times 2$ supercell edges, and 0.150 μ_B induced on all remaining Pt atoms. The AFM [100] ordering of the MnPt₇ structure means that the spin directions are alternating in the (100) second-nearest-neighbor atomic planes the distance of which is a (i.e., one-half the supercell edge $2a$). A similar magnetic ordering of the type [100] has been found experimentally in the Pt 8.8 at% Mn alloy.²⁹ It turns out that the AFM [100] ordering is also the ground-state magnetic ordering of the MnPt₇ nanocomposite. The calculated values of magnetic moments on Mn atoms in MnPt₇ for this AFM ordering are $\pm 3.683 \mu_B$. Unlike for the FM ordering, the magnetic moments induced on Pt atoms are very low in magnitude: ± 0.046 and $\pm 0.010 \mu_B$ for Pt atoms in (100) planes containing Mn atoms and 0 for Pt atoms in (100) planes consisting only of Pt atoms [Fig. 2(a)].

An alternative ordering AFM [111] assumes one uniform spin direction of all electrons in each individual (111) MnPt₃

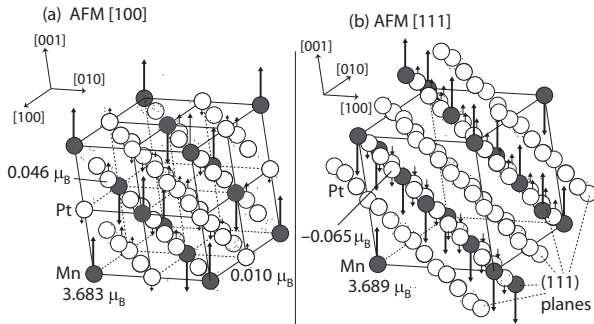


FIG. 2. (a) Calculated ground-state AFM [100] ordering of the MnPt₇ structure. This ordering exhibits the opposite orientation of magnetic moments in the alternative (100) planes containing Mn atoms. Although the crystal structure of MnPt₇ is cubic, antiferromagnetic ordering AFM [100] reduces its symmetry to tetragonal. Calculated magnetic moments induced on Pt atoms are $\pm 0.046 \mu_B$ and $\pm 0.010 \mu_B$ in (100) atomic planes containing Mn atoms. Values of magnetic moments of Mn atoms are $\pm 3.683 \mu_B$. There is no induced magnetic moment on Pt atoms in (100) planes that do not contain any Mn atoms. (b) Calculated alternative AFM [111] antiferromagnetic ordering of the MnPt₇ structure. This ordering exhibits the opposite orientation of magnetic moments in the alternative MnPt₃ (111) planes. There is no induced magnetic moment on Pt atoms in (111) planes consisting of only Pt atoms.

atomic plane. This uniform spin direction is reversed in the neighboring (111) MnPt₃ atomic plane at the distance of $a(2/3)\sqrt{3}$, where, again, a is the lattice constant and $2a$ is the edge of the supercell. The calculated values of magnetic moments in the MnPt₇ compound for this AFM ordering are $\pm 0.065 \mu_B$ and 0 for Pt atoms in the MnPt₃ and pure Pt (111) planes and $\pm 3.689 \mu_B$ for Mn atoms [Fig. 2(b)]. The total energy of the MnPt₇ structure with AFM [111] ordering is higher by 2.6 meV/atom than that of the AFM [100] ground state. The FM ordering exhibits a total energy higher by 12.3 meV/atom than that of the AFM [100] ground state and, therefore, is the least favorable.

This result is similar to the energy difference of 15 meV/atom between the FM and the AFM ordering of MnPt₃.²⁸ Comparing the two values, the antiferromagnetism in MnPt₇ can be stable similarly to the ferromagnetism in MnPt₃. In more detail, one should compare the energy differences between the FM state and the AFM [100] state for both MnPt₃ (35 meV/atom)²⁸ and MnPt₇ (12.3 meV/atom). The ratio of these energy differences equals 2.85 and is similar to the ratio of 2.53 of the Curie temperature of MnPt₃ (380 K) and the temperature of $T_0 = 150$ K below which antiferromagnetism has been detected in the neutron diffraction pattern of a Pt 8.8 at% Mn alloy.²⁹ (This Mn concentration is not very far from the 12.5 at% of MnPt₇.)

The lattice constant a of MnPt₇ and its bulk modulus B , elastic constants, Young moduli, theoretical tensile and compressive strengths $\sigma_{\max,0}$, and corresponding maximum strains $\varepsilon_{\max,0}$ for different magnetic orderings are presented in Table III. It can be seen that the values of the elastic constants and maximum tensile and compressive stresses lie in between the values of elemental Pt and MnPt₃. The lattice constant a is reduced by 0.5%, and the bulk modulus B by 8.7%, compared to those of elemental Pt. On the other hand, the values of the

TABLE III. Lattice constant a , bulk modulus B , elastic constants c_{11} , c_{12} , and c_{44} , Young moduli E_{100} and E_{111} , maximum tensile and compressive stress $\sigma_{\max,0}$, and corresponding strain $\varepsilon_{\max,0}$ for different magnetic orderings in the MnPt₇ structure. Positive values of $\sigma_{\max,0}$ and $\varepsilon_{\max,0}$ correspond to a tension; negative values, to a compression. AFM, antiferromagnetic; FM, ferromagnetic.

	AFM [100]	AFM [111]	FM
a (Å)	3.894	3.894	3.895
B (GPa)	289.3	287.0	287.7
c_{11} (GPa)	379.8	379.6	378.2
c_{12} (GPa)	244.0	240.7	242.4
c_{44} (GPa)	110.7	109.2	107.9
$(c_{11} - c_{12})/2$ (GPa)	68	69	68
E_{100} (GPa)	189	193	189
E_{111} (GPa)	295	291	288
$\sigma_{\max,0} \langle 100 \rangle$ (GPa)	35.38 (−11.43)		35.41 (−11.38)
$\varepsilon_{\max,0} \langle 100 \rangle$ (GPa)	0.310 (−0.109)		0.323 (−0.107)
$\sigma_{\max,0} \langle 111 \rangle$ (GPa)	30.13 (−40.58)		29.68 (−38.54)
$\varepsilon_{\max,0} \langle 111 \rangle$ (GPa)	0.235 (−0.144)		0.220 (−0.141)

shear moduli $(c_{11} - c_{12})/2$ and c_{44} increase by about 21% and 34% with respect to those of elemental Pt and the values of the Young moduli E_{100} and E_{111} increase by 19% and 29%, respectively.

The value of maximum compressive stress for MnPt₇, $\sigma_{\max,0} \langle 100 \rangle = -11.43$ GPa, lies in between the values of -7.83 GPa for elemental Pt and -16.53 GPa for MnPt₃ (Figs. 3 and 9). Similarly to the case of the Pt matrix, the MnPt₇ compound exhibits a face-centered cubic structure. A larger compressive deformation of MnPt₇ along the $\langle 100 \rangle$ direction can result in a body-centered tetragonal or even in a body-centered cubic structure (at constant volume, the bcc structure corresponds to $\varepsilon = -0.206$). However, the increase in $\sigma_{\max,0} \langle 100 \rangle$ by 46% compared to elemental Pt indicates that the presence of Mn atoms hinders the change of shape of the Mn-doped Pt matrix. Maximum tensile stresses in the $\langle 111 \rangle$ and $\langle 100 \rangle$ directions are larger by 6% and 2%, respectively, for MnPt₇ than for the elemental platinum matrix. The increase in the maximum compressive stress $\sigma_{\max,0} \langle 111 \rangle$ is 8.8% compared to that for elemental Pt. Usually, the maximum compressive stress $\sigma_{\max,0}$ corresponds to the theoretical compressive strength, if no other stability condition is violated before reaching the deformation $\varepsilon_{\max,0}$.^{34,35,44} The corresponding maximum deformation $\varepsilon_{\max,0} \langle 111 \rangle$ is lower by 7.7% in MnPt₇ than in elemental Pt. We conclude that the MnPt₇ thin film grown on the Pt(111) substrate¹⁹ (sufficiently thick so that it can exhibit bulk properties of MnPt₇) should be more resistant against compression than the underlying platinum substrate. A compressive load is most typically applied within a hardness test. Coating platinum metal with MnPt₇ can be of technological use for platinum hardening as an alternative to alloying platinum with iridium.

The effect of magnetic ordering on the theoretical tensile and compressive strength of MnPt₇ is small. The only notable difference, about 5%, is between the values of $\sigma_{\max,0} \langle 111 \rangle$ for its FM and its AFM [100] ordering (Fig. 4). When the MnPt₇ structure is squeezed in the $\langle 111 \rangle$ direction, the total energy difference between the AFM [100] and the FM configuration

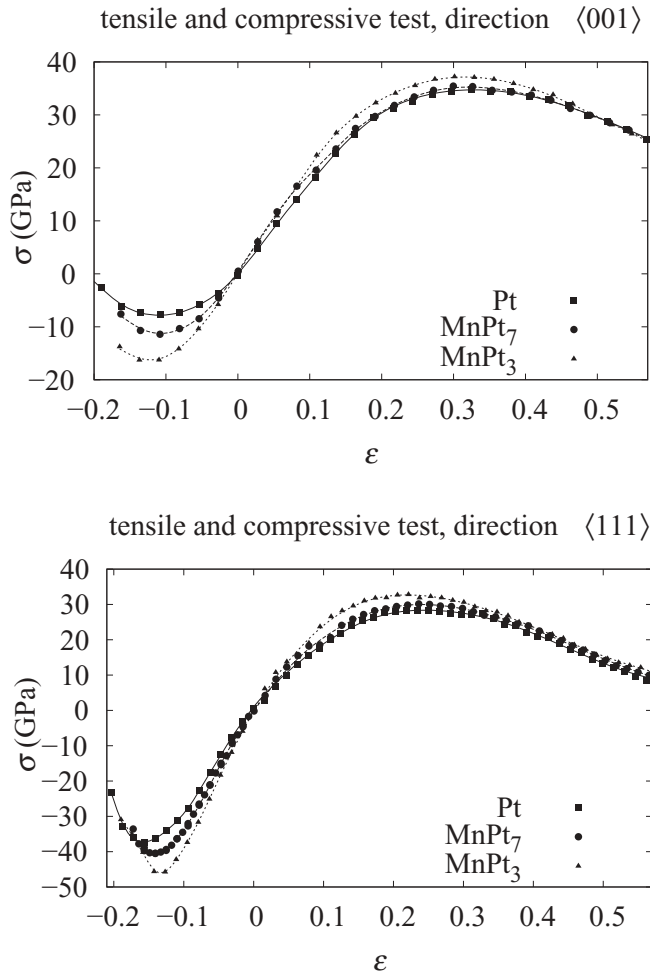


FIG. 3. Variation of tensile and compressive stress σ at zero biaxial stress with respect to the uniaxial deformation ϵ along the $\langle 100 \rangle$ direction (top) and along the $\langle 111 \rangle$ direction (bottom).

decreases from 12.3 meV/atom for $\epsilon = 0$ to 7.2 meV/atom for $\epsilon = \epsilon_{\max,0} \langle 111 \rangle$ [see Fig. 4(b)].

Although the crystal structure of MnPt₇ is cubic, the AFM [100] ordering reduces its symmetry to tetragonal. Strictly speaking, the maximum tensile and compressive stresses $\sigma_{\max,0}$ were computed only along the [100] direction and not along the other [010] and [001] directions. However, as the magnetic ordering turned out to have a negligible impact on the values of both tensile and compressive stress $\sigma_{\max,0}$ [100], we may replace $\sigma_{\max,0}$ [100] with $\sigma_{\max,0} \langle 100 \rangle$.

The variation of tensile and compressive stress σ at zero biaxial stress with the deformation ϵ for both directions is presented in Fig. 3.

D. MnPt₁₅

In this section we propose a $2 \times 2 \times 2$ Pt supercell with some sites preferentially occupied by Mn atoms. This allows us to model an ordered structure with a 6.25% manganese concentration, which we further denote as MnPt₁₅. Here the Mn atoms are always located at the eight corners of the $2 \times 2 \times 2$ supercell, and additionally, either they may occupy the centers of the two faces of the supercell [Fig. 5(a)] or the body

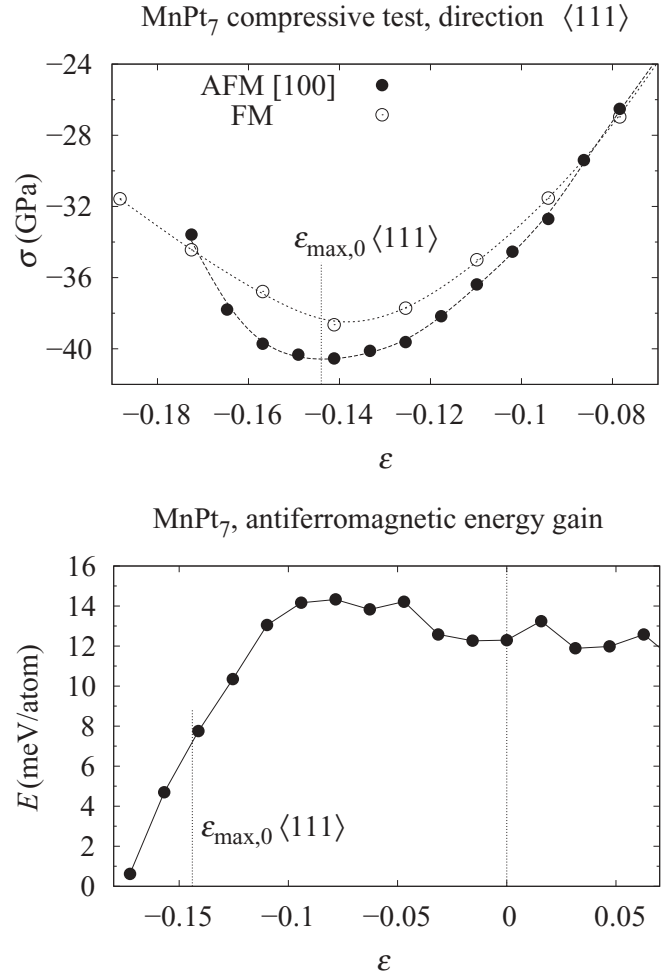


FIG. 4. Top: A detail of the variation of compressive stress σ with the deformation ϵ along the $\langle 111 \rangle$ direction of MnPt₇. Bottom: Variation of the total energy gain due to the antiferromagnetic ordering, AFM [100], compared to the ferromagnetic ordering, FM, with the deformation ϵ along the $\langle 111 \rangle$ direction.

center of the supercell [Fig. 5(b)] or they may be located at the centers of the supercell edges [Fig. 5(c)]. They represent natural nanocomposites which are further denoted as “base centered,” “body centered,” and “nanochains,” respectively.

The base-centered configuration is represented by striped Mn nanochains along the $\langle 110 \rangle$ directions embedded in the Pt matrix. The body-centered configuration exhibits Mn nanochains along the $\langle 111 \rangle$ directions, and, finally, the nanochain configuration is represented by Mn nanochains along the [100] direction in the Pt matrix (see Fig. 5).

Our calculations reveal that the ground state of the MnPt₁₅ structure is the base-centered configuration with AFM ordering (see Table IV and Fig. 6). The calculated values of magnetic moments on Mn atoms are $\pm 3.538 \mu_B$ and the magnetic moments induced on platinum atoms amount to $\pm 0.043 \mu_B$ (Pt atom at the center of the supercell and four atoms at the centers of the supercell edges) and to $\pm 0.012 \mu_B$ (Fig. 6). The Pt atoms positioned in the centers of faces of the $2 \times 2 \times 2$ supercell have zero calculated magnetic moment.

Interestingly enough, our calculation of an alternative magnetic ordering in the base-centered configuration with all

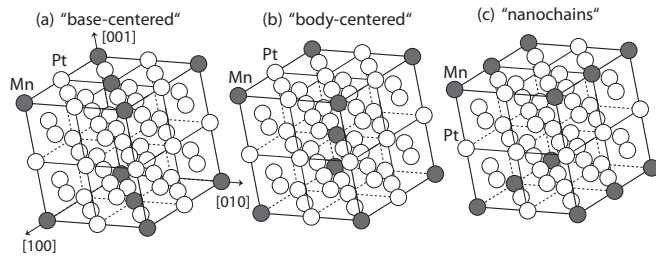


FIG. 5. (a) “base-centered,” (b) “body-centered,” and (c) “nanochains” structures of MnPt_{15} . Mn nanochains are oriented along (a) the $\langle 110 \rangle$, (b) the $\langle 111 \rangle$, and (c) the $[100]$ directions.

Mn spins pointing in one direction results in a *ferrimagnetic* state with all Mn moments of $+3.586 \mu_B$ oriented parallel and the induced moments of $-0.142 \mu_B$ on Pt atoms in the centers of faces of the $2 \times 2 \times 2$ supercell opposing the Mn moments. Other Pt atoms possess induced magnetic moments between $+0.038 \mu_B$ and $+0.103 \mu_B$. The energy of this ferrimagnetic state is higher by 3.3 meV/atom than that of the AFM ground state. This is less than the 12.3 meV/atom for MnPt_7 with 12.5 at% Mn content. If we assume a simple linear dependence of the AFM energy gain on Mn content, we arrive at an AFM energy gain of 6.972 meV/atom for the Pt 8.8 at% Mn alloy. For this alloy, the AFM pattern has been observed by neutron diffraction below 150 K.²⁹ Supposing that the calculated AFM energy gain is proportional to the temperature below which antiferromagnetism can be observed, we estimate that MnPt_7 should exhibit AFM ordering below 265 K.

Further, our calculations can explain the experimentally observed jump of the extrapolated Curie temperature Θ from -45 K at 10 at% Mn to 100 K at 15 at% Mn in Pt-rich Mn-Pt alloys.⁴⁵ If Mn atoms occupied only the corners of the $2 \times 2 \times 2$ supercell, then the Mn content of such a structure would be 3.125 at%. With increasing Mn content, the next Mn atoms preferably occupy the centers of faces of the $2 \times 2 \times 2$ supercell (see energy differences in Table IV). Thus, additional Mn atoms start to build up MnPt_{15} and later, when the Mn content exceeds 6.25 at%, a MnPt_7 structure with a predominant AFM spin arrangement. According to our calculations, antiferromagnetism is still preferred in the MnPt_7 structure with a Mn content of 12.5 at%. A further increase in the Mn content supplies additional Mn atoms to the Pt matrix that now occupy the centers of edges and body center of the $2 \times 2 \times 2$ supercell. However, this means that the extra Mn atoms above a 12.5 at% Mn content start to build up the L1_2 structure of MnPt_3 , which is FM. Consequently, the

TABLE IV. Lattice constant a , bulk modulus B , and energy E per atom with respect to the antiferromagnetic (AFM) “base-centered” ground-state structure for different structures and magnetic orderings of MnPt_{15} .

	Body-centered		Base-centered		Nanochains	
	FM	AFM	FM	AFM	FM	AFM
a (Å)	3.904	3.904	3.905	3.905	3.905	3.905
B (GPa)	307.1	306.8	307.5	306.3	305.1	304.9
E (meV/atom)	5.1	5.9	3.3	0.0	4.6	4.6

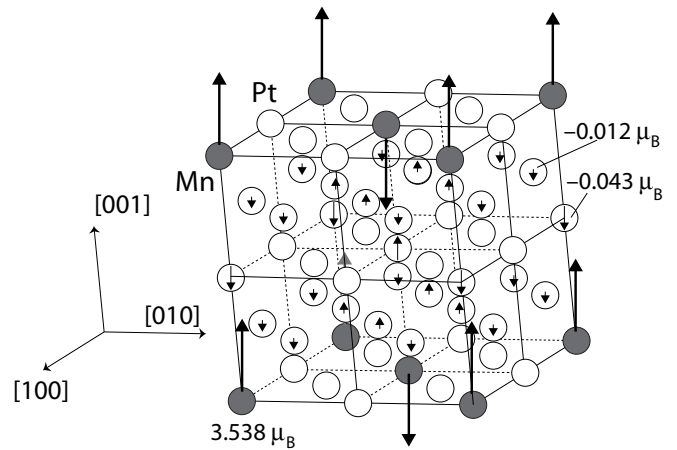


FIG. 6. Ground-state antiferromagnetic ordering of the MnPt_{15} structure in the “base-centered” configuration. The unit cell exhibits a tetragonal symmetry. Mn atoms in the second-nearest-neighbor (100) planes have alternative spin directions.

extrapolation of the Curie temperature Θ jumps from negative to positive values when the Mn content in the Pt matrix exceeds 12.5 at%.

Besides the calculated ferrimagnetic state of the base-centered configuration, similar screening of the Mn magnetic moment by Pt-induced moments can also be found for ferrimagnetic states of the higher-energy body-centered and nanochains configurations. The nanochains nanocomposite has two possible magnetic states (ferrimagnetic and AFM) that are practically degenerate. On the other hand, the body-centered nanocomposite moderately prefers a ferrimagnetic ordering. The calculated screening of the Mn magnetic moments by induced magnetic moments at Pt atoms in the ferrimagnetic configurations of MnPt_{15} indicates that the Mn spins can be coupled through the surrounding Pt atoms, similarly to the way in which spins of Mn atoms in dimers on a CuN substrate can be coupled through nitrogen atoms.¹⁷

The preference for a ferrimagnetic state in MnPt_{15} over an FM state could further indicate that the lack of a sixfold symmetry axis in the $\langle 111 \rangle$ direction in MnPt_{15} could energetically favor a noncollinear magnetic structure. An analogy for this can be found in Mn corrals deposited on a Pt(111) substrate. While corrals arranged in regular hexagons exhibit a collinear AFM ordering, in corrals of irregular shape a noncollinear magnetic ordering⁴⁶ has been found.

From this we further conclude that employing a collinear magnetism for MnPt_7 with a $\langle 111 \rangle$ sixfold symmetry axis is correct, at least as a first approximation. Our AFM calculations for MnPt_{15} nanocomposites can describe, in the first approximation, a spin wave with a wavelength equal to the edge of the $2 \times 2 \times 2$ supercell. Such a spin wave is supposed to be present in MnPt_{15} similarly to that detected experimentally in a Pt 8.8 at% Mn alloy.²⁹ In the general case for MnPt_{15} , the positions of atoms should be relaxed in order to prove the stability of the proposed structure. This issue becomes important when a noncollinear description is used, as, for example, in calculations of the electronic structure of α -manganese⁴⁷ or Mn clusters. However, we may regard the MnPt_{15} nanocomposites as substitutional solid solutions

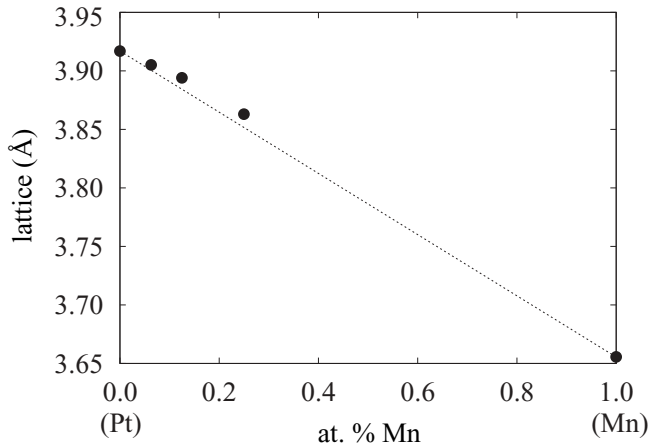


FIG. 7. Variation of the lattice constant of the studied ground-state structures with the manganese concentration. The hypothetical value of 3.655 Å for the “fcc” lattice constant of α -Mn was estimated from Ref. 48 using the experimental value of 8.914 Å for the α -Mn lattice constant.

exhibiting a Mn superlattice. Thus, the Mn atoms are likely to occupy the fcc sites in the embedding Pt matrix as described above and the displacement from the fcc positions should be very small, if any. It is supposed that noncollinear magnetism should provide a better picture of magnetic interactions in MnPt_{15} . But the energy differences among the base-centered, body-centered, and nanochains configurations of MnPt_{15} should not be substantially altered.

The base-centered and nanochains configurations of MnPt_{15} exhibit a tetragonal symmetry. The relaxation of the cell shape of the base-centered AFM configuration of MnPt_{15} increases the c/a ratio to 1.005 and lowers the total energy by only 0.05 meV/atom. Similarly, relaxation of the FM base-centered configuration as well as of both nanochains configurations changes the tetragonal c/a ratio by less than 0.2% from its cubic value. Also, the shape relaxation of the supercells does not change the energy order of the configurations studied. Therefore, we consider these MnPt_{15} nanocomposites to be cubic and use the cubic notation.

The values of the lattice constant, bulk modulus, and energy per atom with respect to the ground-state AFM base-centered structure for particular structures and magnetic orderings are listed in Table IV. For all structures and magnetic orderings, the values do not differ appreciably. But the lowest total energy value found for the base-centered AFM configuration indicates that Mn atoms prefer to occupy centers of the two faces of the $2 \times 2 \times 2$ supercell.

E. Comparison of MnPt_{15} , MnPt_7 , and MnPt_3 compounds with elemental Pt

As the experimental values of the lattice constants of $\text{Pt}_{1-x}\text{Mn}_x$ alloys with different Mn contents²¹ obey the Vegard law, so do the calculated results (Fig. 7). The values of elastic constants of ground-state structures are exhibited in Fig. 8. The values of theoretical tensile and compressive strengths $\sigma_{\max,0}$ and the corresponding deformations $\varepsilon_{\max,0}$ along the $\langle 100 \rangle$ and $\langle 111 \rangle$ directions are presented in Fig. 9.

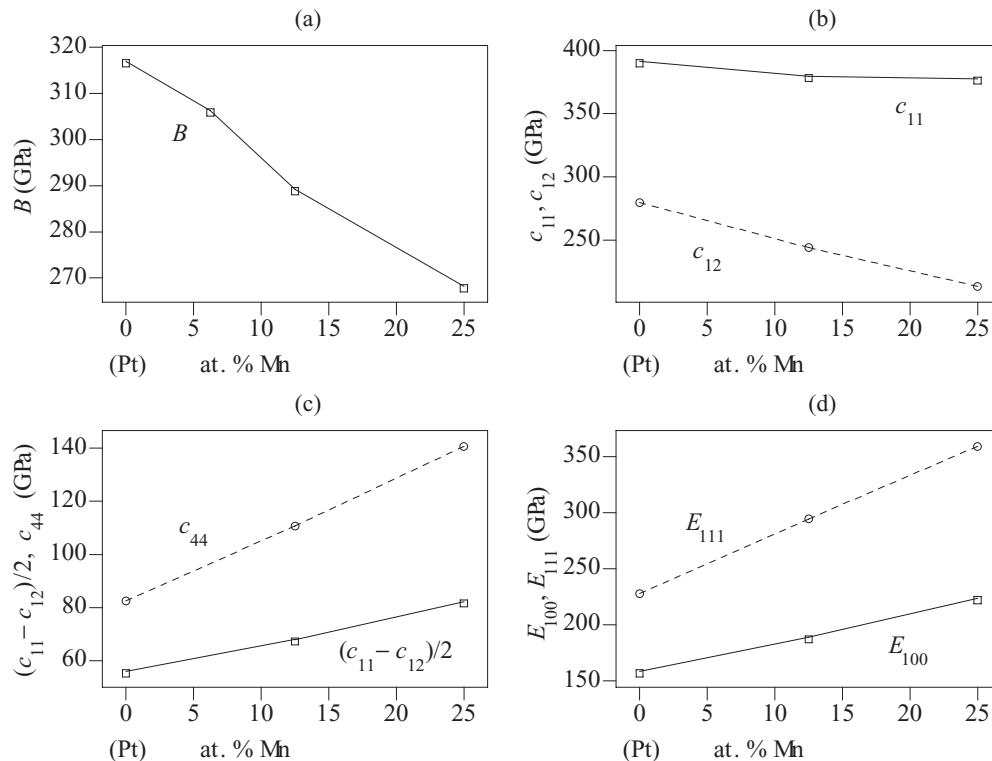


FIG. 8. Variation of elastic properties with manganese content in ground-state structures: (a) bulk modulus B , (b) elastic constants c_{11} and c_{12} , (c) shear moduli $(c_{11} - c_{12})/2$ and c_{44} , and (d) Young moduli E_{100} and E_{111} .

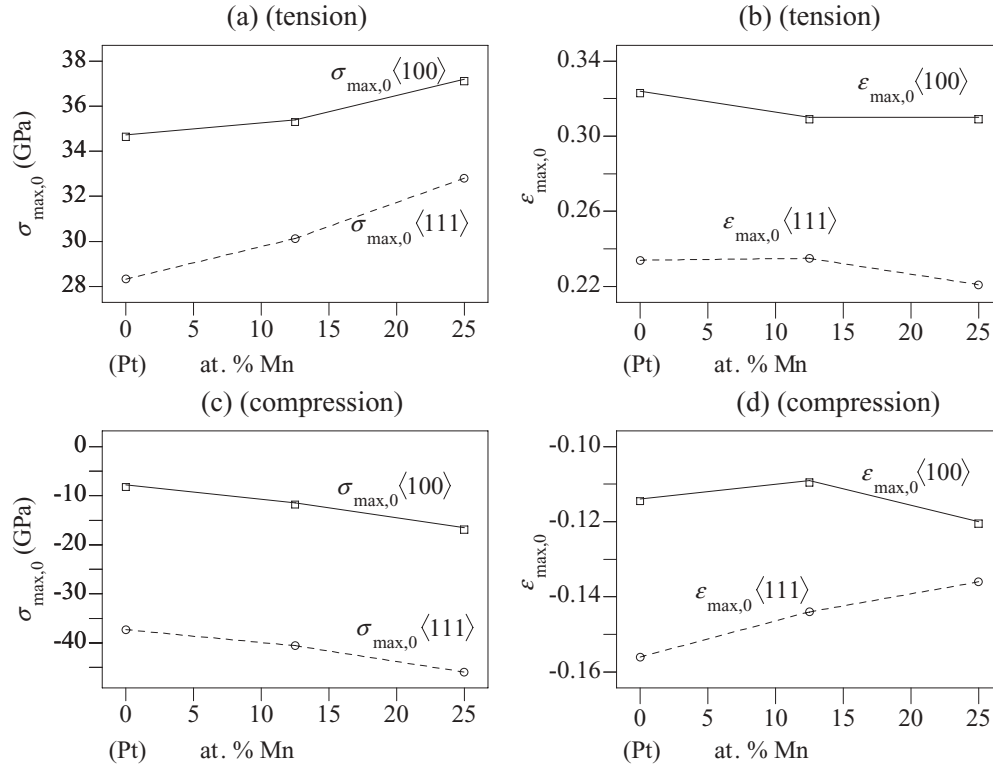


FIG. 9. Variation of tensile and compressive strength $\sigma_{\max,0}$, and the corresponding maximum deformation $\epsilon_{\max,0}$, with manganese content in ground-state structures: (a) theoretical tensile strengths $\sigma_{\max,0} \langle 100 \rangle$ and $\sigma_{\max,0} \langle 111 \rangle$, (b) corresponding strains $\epsilon_{\max,0} \langle 100 \rangle$ and $\epsilon_{\max,0} \langle 111 \rangle$, (c) theoretical compressive strengths $\sigma_{\max,0} \langle 100 \rangle$ and $\sigma_{\max,0} \langle 111 \rangle$, and (d) corresponding strains $\epsilon_{\max,0} \langle 100 \rangle$ and $\epsilon_{\max,0} \langle 111 \rangle$.

From the comparison of elemental Pt to MnPt₁₅, MnPt₇, and MnPt₃, it is clearly seen that the addition of manganese to platinum leads to a little shrinkage of the crystalline lattice and reduces the values of the bulk modulus B as well as of the elastic constants c_{11} and c_{12} . The elastic constant c_{12} is lowered by Mn addition much more than c_{11} is [see Fig. 8(b)]. On the contrary, the shear moduli $(c_{11} - c_{12})/2$ and c_{44} and the Young moduli E_{100} and E_{111} are enhanced. Thus, the Mn atoms make the Pt matrix more compliant to hydrostatic pressure but more resistant to shape deformation. Further, both the tensile and the compressive theoretical strengths $\sigma_{\max,0}$ increase with increasing manganese content, the enhancement of compressive strength being the most pronounced.

IV. CONCLUSIONS

In summary, we have calculated mechanical and magnetic properties of MnPt₃, MnPt₇, and MnPt₁₅ linear nanocomposites and of elemental Pt as a reference. We have found that the addition of manganese atoms makes the platinum matrix softer with respect to hydrostatic loading and induces a higher resistance to deformation of its shape. In other words, the lattice constant a and bulk modulus B decrease with increasing Mn content, while, on the other hand, the values of the shear moduli $(c_{11} - c_{12})/2$ and c_{44} and the Young moduli E_{100} and E_{111} increase. The most pronounced change is a steep increase in the maximum compressive stress $\sigma_{\max,0}$ in the $\langle 100 \rangle$ direction ($\sigma_{\max,0} \langle 100 \rangle$). The maximum

compressive stress $\sigma_{\max,0}$ in the $\langle 111 \rangle$ direction and maximum tensile stress $\sigma_{\max,0}$ in both the $\langle 100 \rangle$ and the $\langle 111 \rangle$ directions increase with the manganese content too. On the other hand, the type of magnetic ordering does not have much impact on the mechanical properties of MnPt₇, except for a small enhancement in the maximum compressive stress $\sigma_{\max,0} \langle 111 \rangle$ due to the AFM ordering in its ground state. On the basis of our calculations we expect that antiferromagnetism in MnPt₇ could be observed below 265 K.

Our calculations further detected that preferential occupation sites of Mn atoms in a Pt matrix are the corners and centers of faces of a $2 \times 2 \times 2$ Pt supercell. A little bit higher energy, about 5 meV/atom, is required if Mn atoms should occupy the corners and centers of edges of the $2 \times 2 \times 2$ supercell. By this model we explained the experimentally observed magnetic behavior of Pt-rich Pt-Mn alloys. In MnPt₇ and in structures with a lower Mn content in the Pt matrix, AFM interactions dominate. However, ferromagnetism starts to apply in structures with a Mn content higher than 12.5 at% because the additional Mn atoms begin to occupy the centers of edges and body center of the $2 \times 2 \times 2$ supercell, thus building up local configurations of MnPt₃ with prevailing FM interactions.

ACKNOWLEDGMENTS

This research was supported by the Ministry of Education of the Czech Republic (Project No. COST OC10008 and No. COST LD12037), the Grant Agency of the Czech

Republic (Project No. P108/12/0311), the Grant Agency of the Academy of Sciences of the Czech Republic (Project No. IAA100100920), Project CEITEC—Central European Institute of Technology (No. CZ.1.05/1.1.00/02.0068) of the European Regional Development Fund, and the Academy of Sciences of the Czech Republic (Institutional Project No. RVO:68081723). The access to the MetaCentrum computing facilities provided

under the program “Projects of Large Infrastructure for Research, Development, and Innovations” (No. LM2010005), funded by the Ministry of Education of the Czech Republic, is greatly appreciated. We are also grateful for the access to the computing facilities of the Institute for Theoretical Computer Science in Plzeň provided under Research Project No. MSMT 1M0545.

*Corresponding author. kana@ipm.cz

†sob@chemi.muni.cz, mojmir@ipm.cz

- ¹D. C. Lee, A. Ghezelbash, C. A. Stowell, and B. A. Korgel, *J. Phys. Chem. B* **110**, 20906 (2003).
- ²P. M. Oppeneer, V. N. Antonov, T. Kraft, H. Eschrig, A. N. Yaresko, and A. Y. Perlov, *Solid State Commun.* **94**, 255 (1995).
- ³Y. Kang and C. B. Murray, *J. Am. Chem. Soc.* **132**, 7568 (2010).
- ⁴S. Mourdikoudis, A. Shavel, B. Rodríguez-González, C. Serra, K. Simeonidis, M. Angelakeris, C. Dendrinou-Samara, and O. Kalogirou, *Polyhedron* **28**, 3284 (2009).
- ⁵A. J. Bradley and J. Thewlis, *Proc. R. Soc. London A* **115**, 456 (1927).
- ⁶J. Guevara, A. M. Llois, F. Aguilera-Granja, and J. M. Montejaño-Carrizales, *Phys. Lett. A* **325**, 144 (2004).
- ⁷M. Kabir, A. Mookerjee, and D. G. Kanhere, *Phys. Rev. B* **73**, 224439 (2006).
- ⁸J. Mejía-López, A. H. Romero, M. E. Garcia, and J. L. Morán-López, *Phys. Rev. B* **74**, 140405 (2006).
- ⁹M. J. Piotrowski, P. Piquini, and J. L. F. Da Silva, *Phys. Rev. B* **81**, 155446 (2010).
- ¹⁰J. C. Tung and G. Y. Guo, *Phys. Rev. B* **76**, 094413 (2007).
- ¹¹C. Ataca, S. Cahangirov, E. Durgun, Y.-R. Jang, and S. Ciraci, *Phys. Rev. B* **77**, 214413 (2008).
- ¹²M. Zelený, M. Šob, and J. Hafner, *Phys. Rev. B* **80**, 144414 (2009).
- ¹³M. Cheeseman, R. J. V. Zee, H. L. Flanagan, and W. Weltner, *J. Chem. Phys.* **92**, 1553 (1990).
- ¹⁴P. P. Infelta, M. Gratzel, and J. K. Thomas, *J. Phys. Chem.* **78**, 190 (1974).
- ¹⁵K. D. Bier, T. L. Haslett, A. D. Kirkwood, and M. Moskovits, *J. Chem. Phys.* **89**, 6 (1988).
- ¹⁶A. D. Kirkwood, K. D. Bier, J. K. Thompson, T. L. Haslett, A. S. Huber, and M. Moskovits, *J. Phys. Chem.* **95**, 2644 (1991).
- ¹⁷C.-Y. Lin and B. A. Jones, *Phys. Rev. B* **83**, 014413 (2011).
- ¹⁸H. Okamoto and J. F. Smith, *J. Phase Equilib.* **24**, 582 (2003).
- ¹⁹S. Gallego, C. Ocal, M. C. Muñoz, and F. Soria, *Phys. Rev. B* **56**, 12139 (1997).
- ²⁰M. Takahashi, T. Sembiring, M. Yashima, T. Shishido, and K. Ohshima, *J. Phys. Soc. Jpn.* **71**, 681 (2002).
- ²¹T. Sembiring, M. Takahashi, K. Ota, T. Shishido, and K. Ohshima, *J. Phys. Soc. Jpn.* **71**, 2459 (2002).
- ²²T. Sembiring, D. K. Saha, M. Takahashi, T. Shishido, and K. Ohshima, *J. Phys. Soc. Jpn.* **72**, 107 (2003).
- ²³M. Hansen, *Constitution of Binary Alloys* (McGraw-Hill, New York, 1958).
- ²⁴K. W. Wierman, J. N. Hilfiker, R. F. Sabiryanov, S. S. Jaswal, R. D. Kirby, and J. A. Woollam, *J. Appl. Phys.* **81**, 5674 (1998).
- ²⁵K. W. Wierman, J. N. Hilfiker, R. F. Sabiryanov, S. S. Jaswal, R. D. Kirby, and J. A. Woollam, *Phys. Rev. B* **55**, 3093 (1997).
- ²⁶E. T. Kulatov, Y. A. Uspensky, and S. V. Halilov, *J. Magn. Magn. Mater.* **154**, 12 (1996).
- ²⁷M. Rajagopalan, *Physica B* **405**, 2516 (2010).
- ²⁸S. C. Hong, *J. Korean Phys. Soc.* **53**, 1525 (2008).
- ²⁹M. Takahashi, S. Yoshimi, K. I. Ohshima, and Y. Watanabe, *Phys. Rev. B* **61**, 3528 (2000).
- ³⁰P. Blaha, K. Schwarz, G. K. H. Madsen, D. Kvasnicka, and J. Luitz, *WIEN2k, An Augmented Plane Wave Plus Local Orbitals Program for Calculating Crystal Properties* (Vienna University of Technology, Vienna, 2007).
- ³¹D. M. Ceperley and B. J. Alder, *Phys. Rev. Lett.* **45**, 566 (1980).
- ³²S. Cottenier, *Density Functional Theory and the Family of (L)APW-Methods: A Step-by-Step Introduction* (Instituut voor Kern- en Stralingsfysica, K.U. Leuven, Belgium, 2004).
- ³³J. F. Nye, *Physical Properties of Crystals: Their Representation in Tensors and Matrices* (Oxford University Press, New York, 1985).
- ³⁴M. Šob, L. G. Wang, and V. Vitek, *Mater. Sci. Eng. A* **234-236**, 1075 (1997).
- ³⁵M. Šob, M. Friák, D. Legut, J. Fiala, and V. Vitek, *Mater. Sci. Eng. A* **387-389**, 148 (2004).
- ³⁶D. R. Lide, *Handbook of Chemistry and Physics* (CRC Press, Boca Raton, FL, 2005).
- ³⁷M. Černý and J. Pokluda, *Phys. Rev. B* **76**, 024115 (2007).
- ³⁸M. Černý and J. Pokluda, *Phys. Rev. B* **82**, 174106 (2010).
- ³⁹M. I. Haftel and K. Gall, *Phys. Rev. B* **74**, 035420 (2006).
- ⁴⁰S. J. Pickart and R. Nathans, *J. Appl. Phys.* **33**, 1336 (1962).
- ⁴¹R. J. Lange, S. J. Lee, D. W. Lynch, P. C. Canfield, B. N. Harmon, and S. Zollner, *Phys. Rev. B* **58**, 351 (1998).
- ⁴²M. Kumar, T. Nautiyal, and S. Auluck, *J. Alloys Compd.* **486**, 60 (2009).
- ⁴³P. Villars and L. Calvert, *Pearson's Handbook of Crystallographic Data for Intermetallic Phases* (ASM International, Materials Park, OH, 1991).
- ⁴⁴M. Černý, M. Šob, J. Pokluda, and P. Šandera, *J. Phys.: Condens. Matter* **16**, 1045 (2004).
- ⁴⁵E. F. Wassermann, *Physica B + C* **109-110**, 1936 (1982).
- ⁴⁶M. S. Ribeiro, G. B. Correa, A. Bergman, L. Nordström, O. Eriksson, and A. B. Klautau, *Phys. Rev. B* **83**, 014406 (2011).
- ⁴⁷D. Hobbs, J. Hafner, and D. Spišák, *Phys. Rev. B* **68**, 014407 (2003).
- ⁴⁸C. S. Barrett and T. B. Massalski, *Structure of Metals: Crystallographic Methods, Principles and Data* (Pergamon, New York, 1980).